

# SALT observations of the supernova remnant MCSNR J0127–7332 and its associated Be X-ray binary SXP 1062 in the SMC

V. V. Gvaramadze,<sup>1,2,3\*</sup> A. Y. Kniazev,<sup>4,5,1</sup> J. S. Gallagher,<sup>6</sup> L. M. Oskinova,<sup>7,8</sup>

Y.-H. Chu,<sup>9</sup> R. A. Gruendl<sup>10,11</sup> and I. Y. Katkov<sup>12,13,1</sup>

<sup>1</sup>*Sternberg Astronomical Institute, Lomonosov Moscow State University, Universitetskij Pr. 13, Moscow 119992, Russia*

<sup>2</sup>*Space Research Institute, Russian Academy of Sciences, Profsoyuznaya 84/32, Moscow 117997, Russia*

<sup>3</sup>*E. Kharadze Georgian National Astrophysical Observatory, Abastumani 0301, Georgia*

<sup>4</sup>*South African Astronomical Observatory, PO Box 9, 7935 Observatory, Cape Town, South Africa*

<sup>5</sup>*Southern African Large Telescope Foundation, PO Box 9, 7935 Observatory, Cape Town, South Africa*

<sup>6</sup>*Department of Astronomy, University of Wisconsin-Madison, 5534 Sterling, 475 North Charter Street, Madison, WI 53706, USA*

<sup>7</sup>*Institute for Physics and Astronomy, University Potsdam, 14476 Potsdam, Germany*

<sup>8</sup>*Kazan Federal University, Kremlevskaya Str 18, Kazan, Russia*

<sup>9</sup>*Institute of Astronomy and Astrophysics, Academia Sinica (ASIAA), 10617 Taipei, Taiwan*

<sup>10</sup>*Department of Astronomy, University of Illinois at Urbana-Champaign, 1002 W. Green Street, Urbana, IL 61801, USA*

<sup>11</sup>*National Center for Supercomputing Applications, 1205 West Clark St., Urbana, IL 61801, USA*

<sup>12</sup>*New York University Abu Dhabi, P.O. Box 129188, Abu Dhabi, UAE*

<sup>13</sup>*Center for Astro, Particle, and Planetary Physics, NYU Abu Dhabi, PO Box 129188, Abu Dhabi, UAE*

Accepted 2021 March 04. Received 2021 February 18; in original form 2020 August 01

## ABSTRACT

We report the results of optical spectroscopy of the Small Magellanic Cloud supernova remnant (SNR) MCSNR J0127–7332 and the mass donor Be star, 2dFS 3831, in its associated high-mass X-ray binary SXP 1062 carried out with the Southern African Large Telescope (SALT). Using high-resolution long-slit spectra, we measured the expansion velocity of the SNR shell of  $\approx 140 \text{ km s}^{-1}$ , indicating that MCSNR J0127–7332 is in the radiative phase. We found that the observed line ratios in the SNR spectrum can be understood if the local interstellar medium is ionized by 2dFS 3831 and/or OB stars around the SNR. We propose that MCSNR J0127–7332 is the result of supernova explosion within a bubble produced by the stellar wind of the supernova progenitor and that the bubble was surrounded by a massive shell at the moment of supernova explosion. We estimated the age of MCSNR J0127–7332 to be  $\lesssim 10\,000$  yr. We found that the spectrum of 2dFS 3831 changes with orbital phase. Namely, the equivalent width of the  $\text{H}\alpha$  emission line decreased by  $\approx 40$  per cent in  $\approx 130$  d after periastron passage of the neutron star and then almost returned to its original value in the next  $\approx 100$  d. Also, the spectrum of 2dFS 3831 obtained closest to the periastron epoch (about three weeks after the periastron) shows a noticeable emission line of  $\text{He II } \lambda 4686$ , which disappeared in the next about two weeks. We interpret these changes as a result of the temporary perturbation and heating of the disk as the neutron star passes through it.

**Key words:** stars: emission-line, Be – stars: individual: 2dFS 3831 – stars: massive – ISM: supernova remnants – X-rays: binaries.

## 1 INTRODUCTION

A binary system surviving a supernova (SN) explosion of one of its components could evolve into an X-ray binary in

which the compact stellar remnant (neutron star or black hole) accretes material from the normal (massive or low-mass) star. The typical time-scale for the formation of X-ray binaries containing neutron stars of  $\sim 10^6 - 10^8$  yr (e.g. Tauris & van den Heuvel 2006) is one to three orders of magnitude longer than the time-scale for visibility of supernova

\* E-mail: vgvaram@mx.iki.rssi.ru

remnants (SNRs) of  $\sim 10^5$  yr (e.g. Lozinskaya 1992), suggesting that none of such X-ray binaries should be detected within SNRs. However, several neutron star X-ray binaries (NSXRBs) were found to be associated with SNRs, which challenges the traditional view on the formation time-scales for these objects and is still waiting to be explained.

Of the known NSXRB/SNR associations, only one was found in our Galaxy, namely SNR G322.1+00.0/Cir X-1 (Heinz et al. 2013; Linares et al. 2010). Two others were detected in the Small Magellanic Cloud (SMC): MCSNR J0127–7332/SXP 1062 (Hénault-Brunet et al. 2012; Haberl et al. 2012) and MCSNR J0103–7201/SXP 1323 (Gvaramadze, Kniazev & Oskinova 2019). And two more were found in the Large Magellanic Cloud: MCSNR J0536–6735/CXOU J053600.0–673507 (Seward et al. 2012; Corbet et al. 2016; van Soelen et al. 2019) and MCSNR J0513–6724/XMMU J051342.6–672412 (Maitra et al. 2019). Study of these and similar systems could provide useful information on the magnetic and spin properties of young neutron stars, supernova kick velocities, parameters of pre-SN binaries, and evolution of post-SN orbits in NSXRBs (see, e.g., Haberl et al. 2012; González-Galán et al. 2018; Wang & Tong 2020; Ho et al. 2020).

In this paper, we report the results of observations of the SNR MCSNR J0127–7332 in the wing of the SMC and the mass donor star, 2dFS 3831, in its associated NSXRB SXP 1062 with the Southern African Large Telescope (SALT). In Section 2, we briefly review what is already known about these objects. Section 3 describes our observations and data reduction. The obtained results are presented in Section 4 and discussed in Section 5. We summarise in Section 6.

## 2 MCSNR J0127–7332/SXP 1062: OBSERVATIONAL DATA

The NSXRB SXP 1062 was discovered by Hénault-Brunet et al. (2012) in the wing of the SMC in the course of observations of the massive star-forming region NGC 602 with *Chandra* and *XMM-Newton*. Like most of NSXRBs in the SMC, SXP 1062 belongs to a class of Be X-ray binaries (BeXBs) that consist of a neutron star accreting from the circumstellar disc of a Be star. The neutron star in SXP 1062 orbits around the B0.5(III)e star 2dFS 3831 (Hénault-Brunet et al. 2012) with an orbital period of  $P_{\text{orb}} \approx 656$  d (Schmidtke, Cowley & Udalski 2012, 2019; see also Section 4.2) and its spin period of  $P_{\text{spin}} = 1062$  s makes SXP 1062 the third longest-period BeXB in the SMC (Haberl & Sturm 2016).

Hénault-Brunet et al. (2012) presented spectra of 2dFS 3831 obtained with the VLT-FLAMES instrument on 2010 October 25 and the multi-fibre 2-degree Field (2dF) instrument of the Anglo-Australian Telescope in 1998 September (blue spectrum) and 1999 September (red spectrum). These spectra showed that the  $H\alpha$  and  $H\beta$  lines are purely in emission and revealed the presence of emission in the cores of other Balmer lines and apparent infilling of the He I absorption lines. Also, emission lines of Fe II  $\lambda 4179$  and Fe II  $\lambda 4233$  and a weak absorption line of He II  $\lambda 4542$  were detected in the VLT-FLAMES spectrum, and a hint of weak He II  $\lambda 4696$  line was found in the 2dF spectrum. González-

Galán et al. (2018) compiled equivalent width (EW) measurements for the  $H\alpha$  line in the spectra of 2dFS 3831 obtained in 1999–2016 and found that its absolute value increased from  $23 \pm 1 \text{ \AA}$  in 1999<sup>1</sup> to  $36.3 \pm 0.6 \text{ \AA}$  in 2014 and then decreased to  $33 \pm 1 \text{ \AA}$  in the next two years after the X-ray outburst in mid-2014 (see also Section 4.2).

Hénault-Brunet et al. (2012) also discovered a SNR around SXP 1062 and presented its  $H\alpha$ , [S II] and [O III] images from the Magellanic Cloud Emission-line Survey (MCELS), and the higher resolution  $H\alpha$  image from the Magellanic Clouds Emission Line Survey 2 (MCELS2). The SNR shell (of angular diameter of  $\approx 2.7$  arcmin) is clearly visible in  $H\alpha$  and [O III], but hardly can be detected in [S II]. This appears unusual because it is believed that in SNRs the intensity ratio of the [S II]  $\lambda\lambda 6716, 6731$  to  $H\alpha$  emission lines should be quite large ( $> 0.4$ ; e.g. Mathewson & Clarke 1973; Fesen, Blair & Kirshner 1985). The low intensity of the [S II] emission lines was interpreted by Hénault-Brunet et al. (2012) as the result of photoionization of the SNR shell and the local interstellar medium (ISM) by 2dFS 3831 and/or by an ionizing radiation from hot massive stars in the star cluster NGC 602 and a rich collection of OB stars within the giant shell SMC-SGS 1 to the north of NGC 602 (Fulmer et al. 2020). The SNR shell is most fully visible in the [O III] image, where its radius varies from  $\approx 75$  arcsec at the northwest rim to  $\approx 90$  arcsec in the opposite direction.

MCSNR J0127–7332 was independently discovered by Haberl et al. (2012). In addition to the MCELS images of the SNR, they also presented its MOST (Molonglo Observatory Synthesis Telescope) 843 MHz radio and *XMM-Newton* X-ray images. In radio the SNR shows a clear shell-like structure of the same size as the optical shell, while in X-rays it appears as a patchy diffuse emission confined within the optical shell. MCSNR J0127–7332 was also observed with the Australia Telescope Compact Array (ATCA) at  $\approx 1500$  MHz (Haberl et al. 2012). By combining the ATCA and MOST data, Haberl et al. (2012) derived a spectral index of the SNR ( $S_\nu \propto \nu^\alpha$ ) of  $\alpha = -0.8 \pm 0.4$ , indicating the non-thermal nature of its radio emission.

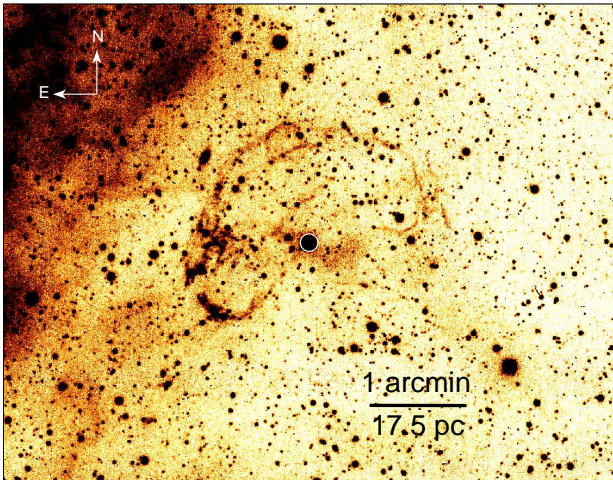
Using the measured peak surface brightness of the northeast rim of MCSNR J0127–7332 and the apparent thickness of the SNR shell of is 5–10 per cent of the shell radius, Hénault-Brunet et al. (2012) derived the number density of the shell and its mass of  $1.3 \pm 0.3 \text{ cm}^{-3}$  and  $250 \pm 100 M_\odot$ , respectively. Then, assuming that MCSNR J0127–7332 is in the Sedov phase, meaning that the kinetic energy of the shell is  $\approx 30$  per cent of the SN explosion energy (assumed to be equal to  $E_0 = 10^{51}$  erg), they derived the expansion velocity of the SNR and its age to be, respectively  $V_{\text{SNR}} = 350 \pm 100 \text{ km s}^{-1}$  and  $t_{\text{SNR}} = (2 - 4) \times 10^4 \text{ yr}$ . Similarly, assuming that the SNR is in the Sedov phase and using the temperature of X-ray emitting plasma of 0.23 keV (obtained from X-ray spectral modelling), Haberl et al. (2012) derived  $t_{\text{SNR}} \approx 1.6 \times 10^4 \text{ yr}$ , which implies  $V_{\text{SNR}} \approx 440 \text{ km s}^{-1}$ .

In Fig. 1, we show the MCELS2  $H\alpha$  image of MCSNR J0127–7332. The SNR appears as an incomplete al-

<sup>1</sup> Note that González-Galán et al. (2018) mistakenly indicated the date of this measurement as 2010 October 25, while actually it was obtained in 1999 September.

**Table 1.** Details of the SALT observations.

Date	Grating	Exposure (sec)	Spectral scale ( $\text{\AA pixel}^{-1}$ )	Spatial scale (arcsec pixel $^{-1}$ )	PA ( $^{\circ}$ )	Slit (arcsec)	Seeing (arcsec)	Spectral range ( $\text{\AA}$ )
2012 October 13	PG2300	400×2	0.35	0.255	123	0.6	3.0	3817–4913
2014 June 27	PG2300	400×2	0.34	0.255	123	1.5	1.3	3814–4904
2014 July 09	PG2300	400×2	0.34	0.255	123	1.5	2.2	3814–4904
2016 November 1	PG2300	1100×4	0.27	0.255	90	1.25	1.6	5900–6760
2018 December 21	PG2300	1500×1	0.26	0.510	125	2.00	2.1	6070–6900
2020 December 24	PG900	1500×1	0.97	0.255	90	1.25	1.2	3619–6708

**Figure 1.** MCELS2  $H\alpha$  image of MCSNR J0127–7332 and the mass donor star 2dFS 3831 (marked with a white circle) of the BeXB SXP 1062. The bright emission to the northeast of the SNR is the  $HII$  region LHA 115-N 90 surrounding the massive star cluster NGC 602.

most circular filamentary shell. The bright star, 2dFS 3831 (marked with a white circle), near the centre of the SNR is the mass donor of SXP 1062. The east (bright) side of the SNR is faced towards the  $HII$  region LHA 115-N 90 excited by the massive star cluster NGC 602. This brightness asymmetry could be caused by increase in the number density of the local interstellar medium (ISM) towards the  $HII$  region or by interaction of the SN blast wave with a gas outflow driven by massive stars in NGC 602. In both cases, the blast wave would be somewhat slower in the east direction, which can explain why 2dFS 3831 is offset from the geometric centre of the SNR towards its more bright edge.

In what follows, we assume that the SMC is located at 60 kpc (Hilditch, Howarth & Harries 2005). At this distance 1 arcmin corresponds to  $\approx 17.5$  pc. Correspondingly, the linear radius of the SNR is  $R_{SNR} \approx 23$  pc.

### 3 OBSERVATIONS

We obtained long-slit spectra of MCSNR J0127–7332 with the Robert Stobie Spectrograph (RSS; Burgh et al. 2003; Kobulnicky et al. 2003) attached to the SALT (Buckley, Swart & Meiring 2006; O’Donoghue et al. 2006). The observations were carried out in 2016, 2018 and 2020. In 2016,

the spectra were obtained using the PG2300 grating with the spectral resolution FWHM of  $FWHM=1.6 \pm 0.2 \text{ \AA}$ . In 2018, we used the same grating with a wider slit width, resulting in the spectral resolution FWHM of  $2.2 \pm 0.2 \text{ \AA}$ . Hereafter, we will refer to these spectra as high-resolution spectra. In 2020 we obtained one more spectrum using the PG900 grating, which allowed us to cover a much wider spectral range, but with a lower spectral resolution FWHM of  $4.5 \pm 0.5 \text{ \AA}$  (hereafter, a low-resolution spectrum).

In all these observations the slit was placed on 2dFS 3831 and oriented in such a way as to cross the brightest knots in the eastern and southeastern edges of the shell (see Fig. 1 and the bottom right panel of Fig. 2). Namely, in 2016 and 2020 the slit was oriented in the west-east direction, i.e. at a position angle (PA) of  $PA=90^{\circ}$  (measured from north to east), while in 2018 it was oriented at  $PA=125^{\circ}$ . The goal of these observations was to try to determine the expansion velocity of the SNR shell (as we did this for MCSNR J0103–7201; Gvaramadze et al. 2019) and to check whether the  $H\alpha$  line in the spectrum of 2dFS 3831 continues to change its EW.

For wavelength calibration of the spectra an Xe lamp arc spectrum was taken immediately after the science frames. Spectrophotometric standard stars were observed at the same spectral setups for the relative flux calibration.

The obtained spectra were first reduced using the SALT science pipeline (Crawford et al. 2010), and further reduced as described in Kniazev et al. (2008). Calibration of the absolute flux is not possible with SALT because the telescope’s unfilled entrance pupil moves during observations. Still, a relative flux correction to recover the spectral shape can be done using the observed spectrophotometric standards.

We also extracted from the SALT archive three observational sets of 2dFS 3831 obtained in 2012 and 2014. The spectra obtained in 2012 were presented in Sturm et al. (2013), while those obtained in 2014 and 2016 were used in Gonzales-Galan et al. (2018) to study changes in  $EW(H\alpha)$  in the spectrum of 2dFS 3831. For this paper, we reduced only blue parts of these spectra and used them to analyse 2dFS 3831 (see Section 4.2). Since the red parts of the spectra cover only the spectral region around the  $H\alpha$  line, in our analysis we just used published values of  $EW(H\alpha)$  from the literature. The spectral resolution FWHMs of the 2012 and 2014 spectra are  $1.2 \pm 0.2$  and  $2.0 \pm 0.3 \text{ \AA}$ , respectively.

Note that Sturm et al. (2013) and Gonzales-Galan et al. (2018; see their table A1) give incorrect positional angles for their observations. The correct ones are given in Table 1 along with other details of all six observations utilized in this paper.

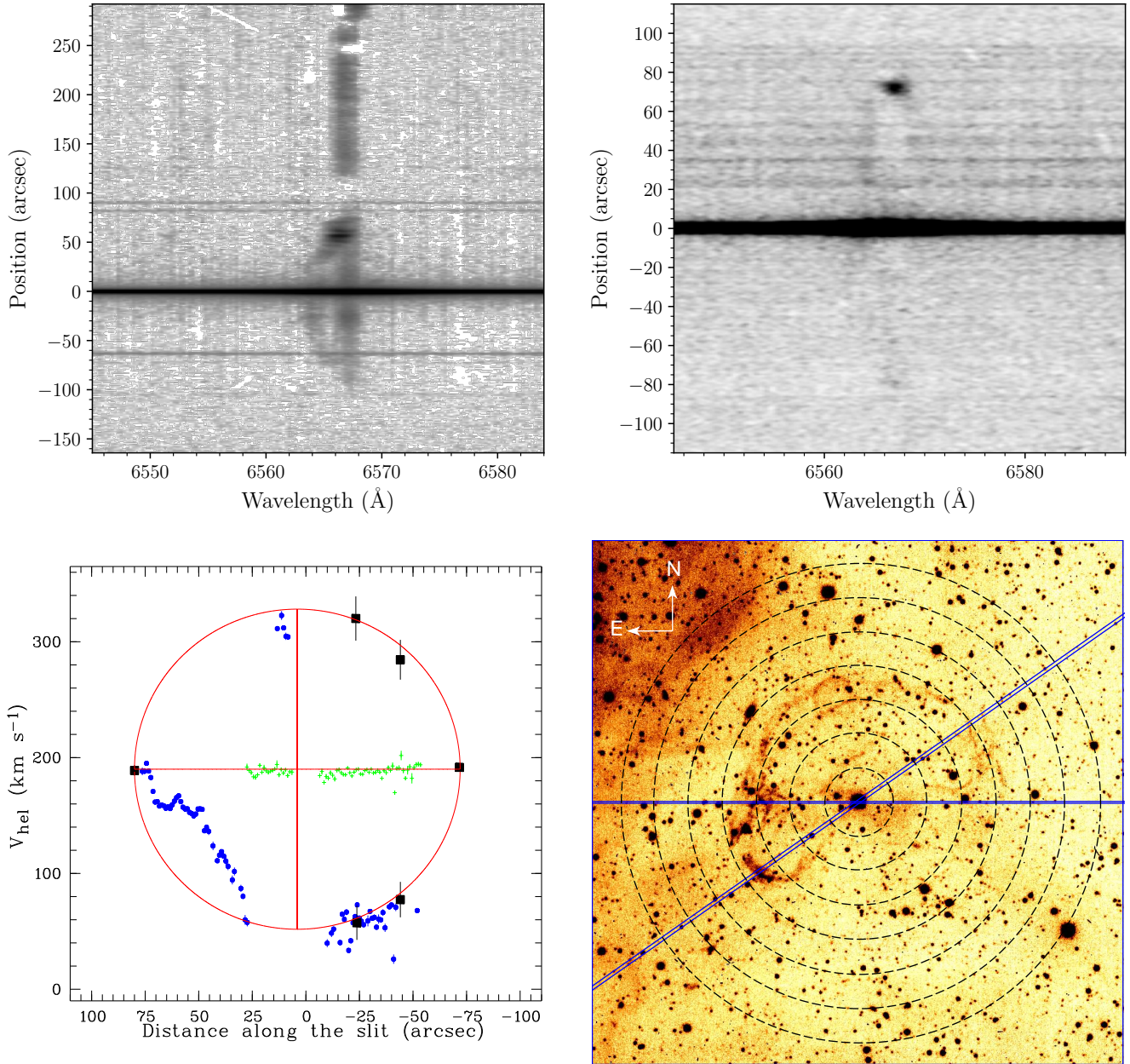


**Figure 2.** Upper panels: Portions of the 2D high-resolution spectra of the SNR shell, showing the H  $\alpha$  emission line intensity along the slits with PA=90° (left-hand panel; east is up and west is down) and PA=125° (right-hand panel; southeast is up and northwest is down). Bottom left-hand panel: H  $\alpha$  heliocentric radial velocity distribution along the slits. Black squares with error bars correspond to measurements at several positions in the 2D spectrum shown in the upper right panel. The (blue) dots with error bars show the heliocentric radial velocity of the shell measured in the 2D spectrum shown in the upper left panel. The (green) crosses show the heliocentric radial velocity of the background H  $\alpha$  emission of  $\approx 188 \pm 6$  km s<sup>-1</sup>. Bottom right-hand panel: MCELS2 H  $\alpha$  image of the SNR MCSNR J0127–7332 centred on 2dFS 3831. The positions of the SALT RSS slits with PA=90° and 125° are shown, respectively, by 1.25 and 2 arcsec wide blue rectangles. Concentric, dashed circles of angular radius in the range from 20 to 140 arcsec with a step of 20 arcsec are added to the image to facilitate its comparison with the 2D spectra. See the text for details.

## 4 RESULTS

### 4.1 MCSNR J0127–7332

In upper panels of Fig.2, we present portions of the 2D high-resolution spectra of the SNR shell obtained for two slit orientations: PA=90° (left-hand panel) and PA=125° (right-hand panel). The left-hand panel shows that the H  $\alpha$

emission along the slit comes from two major components: an almost straight (vertical) component (we attribute it to the background ISM; see below) and a blueshifted arc with a bright knot on its eastern edge (we attribute this component to the near side of the SNR shell). There is also a portion of redshifted (receding) side of the shell at  $\approx +10$  arcsec. The arc-like emission component extends along the slit between  $\approx +75$  and  $-90$  arcsec. The right-hand panel shows that at

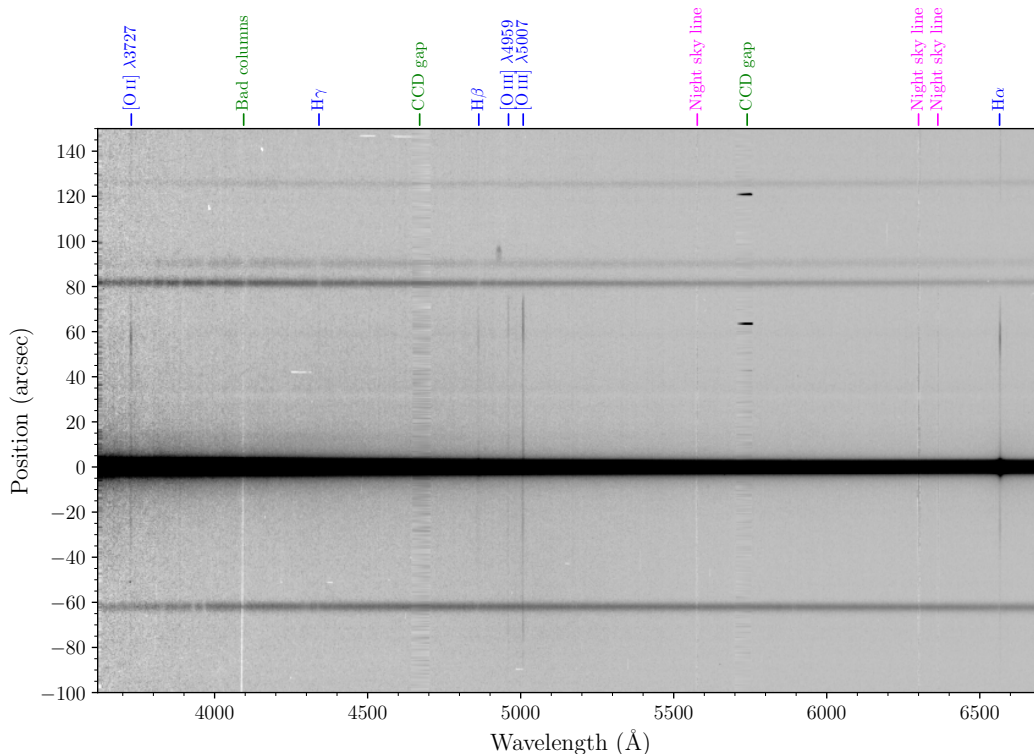


**Figure 3.** 2D low-resolution spectrum of MCSNR J0127–7332 and its environs. Positive offsets are east of 2dFS 3831.

PA=125° we see both the receding and approaching sides of the shell. It also shows a bright knot at  $\approx +75$  arcsec, which corresponds to the southeast edge of the SNR shell. In the northwest direction the shell extends to  $\approx -80$  arcsec. Note that the second spectrum (PA=125°) was taken with an  $\approx 3$  times shorter exposure, an 1.6 time wider slit and about a factor of 1.3 worse seeing (see Table 1). This explains why the background ISM emission is only weakly visible in this spectrum (e.g. at +10 arcsec).

To derive the expansion velocity of the SNR shell,  $V_{\text{sh}}$ , we measured the heliocentric radial velocity,  $V_{\text{hel}}$ , of the H  $\alpha$  line along the slits using the 2D high-resolution spectra. The results of the measurements are plotted in the bottom left panel of Fig. 2. The black squares with error bars show heliocentric radial velocities measured at several positions in the 2D spectrum obtained with the slit oriented at PA=125°. One can see that these data points fit pretty well into the circle. Assuming for the sake of simplicity that the SNR expands spherically symmetric, one finds  $V_{\text{sh}} \approx 138 \pm 5 \text{ km s}^{-1}$  and the systemic velocity of the shell of  $V_{\text{sys}} = 190 \pm 5 \text{ km s}^{-1}$ .

Similarly, we also measured  $V_{\text{hel}}$  using the second 2D high-resolution spectrum (PA=90°). These measurements are plotted in the same panel with (blue) dots with error bars (in most cases the bars are shorter than the size of the dots). In general, they also fall well on the circle, except of data points in the range between  $\approx +30$  and +70 arcsec, where  $V_{\text{hel}}$  shows systematically lower values. This deviation indicates that the east side of the shell expands with a somewhat lower velocity than the opposite one (cf. Section 3), which is consistent with the off-centred location of

2dFS 3831 within the SNR. It could also be caused in part by non-radial motions due to large-scale deformations of the shell, as evidenced by its complex structure on the east side from 2dFS 3831 (see the bottom right panel of Fig. 2). The (green) crosses stretched horizontally from west to east correspond to the straight component of the H  $\alpha$  emission in the 2D high-resolution spectrum with PA=90°. The mean  $V_{\text{hel}}$  of this component of  $\approx 188 \pm 6 \text{ km s}^{-1}$  is equal to  $V_{\text{sys}}$  of the shell and to  $V_{\text{hel}}$  of the H II region to the east of the SNR (see the upper left and the bottom right panels of Fig. 2; cf. Nigra et al. 2008). Thus, we interpret this component as a background emission not related to the SNR.

Fig. 3 shows a portion of the 2D low-resolution spectrum of MCSNR J0127–7332 and its environs. In this spectrum the SNR occupies the area between  $\approx -90$  and +75 arcsec (positive offsets are east of 2dFS 3831). One can see that the spectrum of the SNR is dominated by emission lines of H  $\alpha$ , H  $\beta$ , [O III]  $\lambda\lambda 4959, 5007$  and [O II]  $\lambda 3727$  (a blend of the [O II]  $\lambda\lambda 3726, 3729$  lines), whose intensities are maximum near the eastern edge of the SNR shell. One can also see that the high-excitation [O III] emission lines are confined within boundaries of the SNR, while the [O II] and H  $\alpha$  lines are also visible beyond the SNR at angular distances greater than +120 arcsec, i.e. in the H II region to the east of the SNR (compare with the upper left and bottom right panels of Fig. 2).

The upper panel of Fig. 4 plots the [O III]  $\lambda 5007$ , H  $\beta$  and [O II] line intensity profiles along the slit. It shows that the intensities of the H  $\beta$  and [O II] lines are maximum at the position of the bright knot near the eastern edge of the SNR shell (the region between +50 and +62 arcsec from

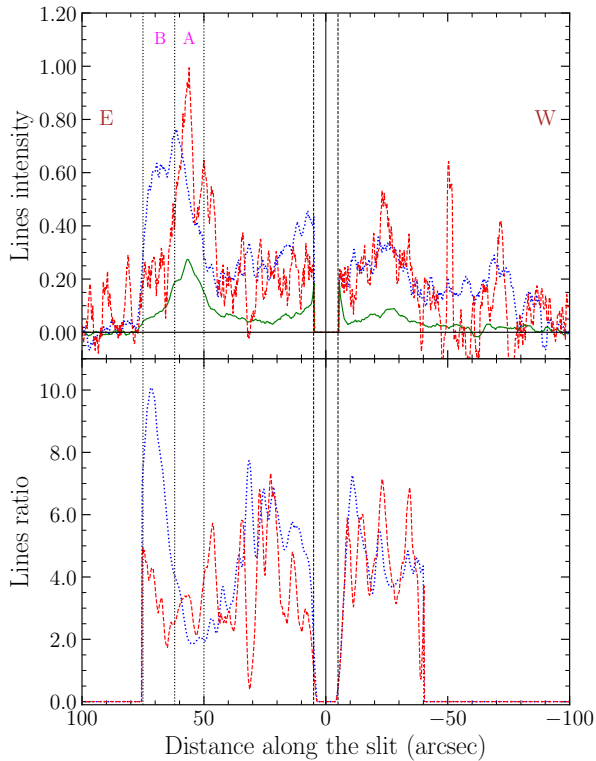


**Figure 4.** Upper panel: [O III]  $\lambda 5007$ ,  $H\beta$  and [O II]  $\lambda 3727$  line intensity profiles along the slit for the low-resolution spectrum, shown, respectively, with blue (dotted), green (solid) and red (dashed) lines. The two vertical strips (bounded by dotted lines) show the regions (region A and region B) of the 2D spectrum from which the 1D spectra shown in Fig. 5 were extracted. Bottom panel: variations of the [O III]/ $H\beta$  and [O II]/ $H\beta$  line ratios along the slit, shown respectively by dotted (blue) and dashed (red) lines. The solid vertical line in both panels corresponds to the position of 2DFS 3831, while the dashed vertical lines at  $\pm 5$  arcsec from the solid line mark the area where the nebular emission was not detected because of the effect of 2DFS 3831. E–W direction of the slit is shown.

2dFS 3831; see also the bottom right panel in Fig. 2) and drop to zero at the edge of the SNR. In contrast to these lines, the intensity of the [O III]  $\lambda 5007$  line reaches its maximum at the outer border of the knot and remains high to the very edge of the shell. Correspondingly, the [O III] to  $H\beta$  line ratio abruptly increases by a factor of about 5 beyond the knot, indicating high excitation conditions in this part of the SNR (see the bottom panel of Fig. 4).

Fig. 5 presents 1D spectra of two regions in the east of the SNR. These spectra were extracted from the 2D low-resolution spectrum by summing up rows in the ranges from +50 to +62 arcsec (hereafter region A) and from +62 to +75 arcsec (hereafter region B). The region A coincides with the bright knot (see Fig. 2), while the region B corresponds to the high-excitation region to the east of the knot. The inserts in Fig. 5 show portions of the 1D high-resolution spectrum (PA=90°) around the  $H\alpha$  line. Besides the  $H\alpha$ ,  $H\beta$ , [O III] and [O II] emission lines, the spectra also show much weaker emission lines due to  $H\gamma$ , [N II]  $\lambda 6584$ , and [S II]  $\lambda\lambda 6716, 6731$ . In the high-resolution spectrum of region A, we also detected the [O I]  $\lambda 6300$  (not shown in Fig. 5) and [N II]  $\lambda 6548$

**Table 2.** Observed line ratios in the low-resolution spectra of two regions in the east side of the SNR. See text for details.

$\lambda_0(\text{\AA})$ Ion	Region A $F(\lambda)/F(H\beta)$	Region B $F(\lambda)/F(H\beta)$
3727 [O II]	$3.54 \pm 0.25$	$3.92 \pm 0.57$
4340 $H\gamma$	$0.25 \pm 0.04$	$0.55 \pm 0.10$
4861 $H\beta$	$1.00 \pm 0.09$	$1.000 \pm 0.16$
4959 [O III]	$0.67 \pm 0.06$	$2.90 \pm 0.35$
5007 [O III]	$2.42 \pm 0.16$	$7.99 \pm 0.92$
6300 [O I]	$0.07 \pm 0.01$	—
6548 [N II]	$0.06 \pm 0.01$	—
6563 $H\alpha$	$2.98 \pm 0.19$	$3.19 \pm 0.36$
6584 [N II]	$0.17 \pm 0.01$	$0.15 \pm 0.03$
6717 [S II]	$0.42 \pm 0.03$	$0.12 \pm 0.03$
6731 [S II]	$0.30 \pm 0.02$	$0.11 \pm 0.02$
$\log([O II]/H\beta)$	$0.55 \pm 0.05$	$0.59 \pm 0.09$
$\log([O III]/H\beta)$	$0.38 \pm 0.05$	$0.90 \pm 0.08$
$\log([O I]/H\alpha)$	$-1.61 \pm 0.06$	—
$\log([N II]/H\alpha)$	$-1.11 \pm 0.04$	$-1.21 \pm 0.09$
$\log([S II]/H\alpha)$	$-0.62 \pm 0.04$	$-1.15 \pm 0.09$

emission lines. All detected lines were measured using programs described in Kniazev et al. (2004) and their observed intensities normalized to  $H\beta$ ,  $F(\lambda)/F(H\beta)$ , are given in Table 2. This table also gives several diagnostic emission line ratios, which can be used to separate SNRs from H II regions and circumstellar nebulae. In these ratios, the symbols [N II] and [S II] mean the sum of the intensities of both lines of the doublet.

From Table 2 it follows that the intensity ratio of the combined [S II] lines against  $H\alpha$  of  $\approx 0.07 - 0.24$  is below the low end of a range of values ( $\geq 0.3 - 0.4$ ) commonly used to separate SNRs from other types of emission nebulae (e.g., Rosado et al. 1983; Gergely et al. 1983; Frew & Parker 2010; Leonidaki, Boumis & Zezas 2013). On the other hand, Kopsacheili, Zezas & Leonidaki (2020) showed that the use of the  $[S II]/H\alpha > 0.4$  criterion leads to a selection effect against evolved SNRs, because the  $[S II]/H\alpha$  ratio produced by their low-velocity ( $\sim 100 \text{ km s}^{-1}$ ) shocks is predominantly  $< 0.4$  (see also Dopita & Sutherland 1996). Moreover, Kopsacheili et al. (2020) found that at subsolar metallicities the use of the  $[S II]/H\alpha > 0.4$  criterion may lead to rejection of about 70 per cent of genuine SNRs. Instead, they proposed to use 2D and 3D diagnostics based on intensity ratios between optical forbidden lines (the ones that are usually stronger in shock-excited nebulae than in photoionized ones) and their closest Balmer lines. Namely, in addition to the [S II]  $\lambda\lambda 6717, 6731$  lines, it was proposed to use the [N II]  $\lambda 6584$ , [O I]  $\lambda 6300$ , [O II]  $\lambda 3727$  and [O III]  $\lambda 5007$  lines as well.

To create diagnostic diagrams, Kopsacheili et al. (2020) used theoretical line ratios from grids of shock-excitation and photoionization models (MAPPINGS III) by Allen et al. (2008), which were calculated for wide ranges of shock velocities (from 100 to 1000  $\text{km s}^{-1}$ ) and magnetic parameters  $B_{\text{ISM}}/n_{\text{ISM}}^{1/2}$  (from  $10^{-4}$  to  $10 \mu\text{G cm}^{3/2}$ ), where  $B_{\text{ISM}}$  and  $n_{\text{ISM}}$  are, respectively, the transverse component of the local ISM magnetic field and the local ISM number density, and different abundances (including that of the SMC). Par-

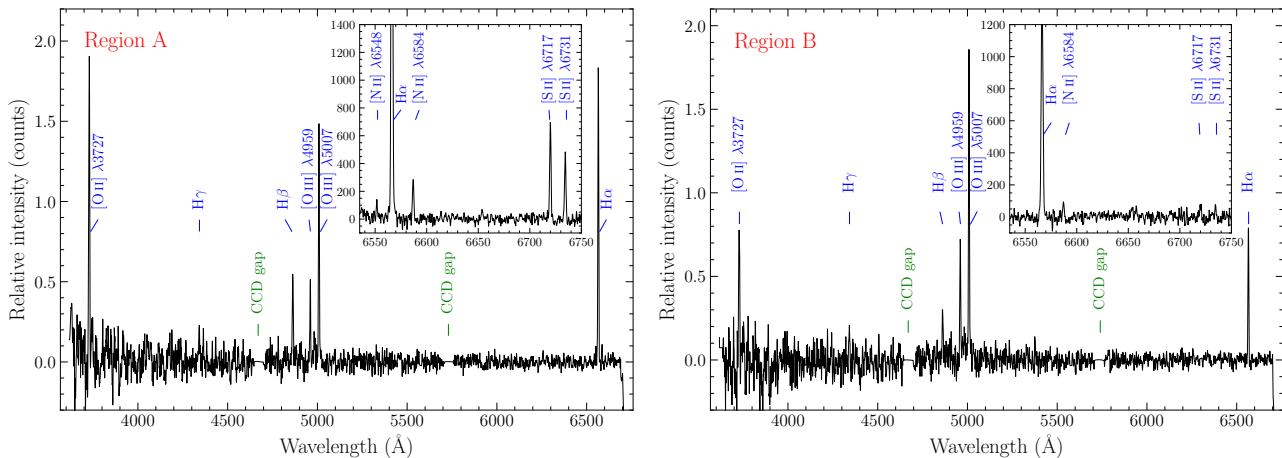


**Figure 5.** 1D low-resolution spectra of two regions in the east of the SNR. The inserts show portions of the high-resolution spectrum around the H  $\alpha$  line. See text for details.

ticularly, their [S II]/H  $\alpha$ –[O I]/H  $\beta$  diagnostic diagram (see their fig. 5) shows that there is a significant fraction of shock models with [S II]/H  $\alpha$  < 0.4. Using line ratios from Table 2, one can see that MCSNR J0127–7332 falls in the SNR locus in all diagnostic diagrams constructed by Kopsacheili et al. (2020; see their figs 4, 5 and 7–11), which supports the classification of MCSNR J0127–7332 as a SNR.

#### 4.2 2dFS 3831

The obtained spectra of 2dFS 3831 were analysed with the FBS (Fitting Binary Stars) software (Kniazev et al. 2020; Katkov et al., in preparation). This software allows to determine parameters of individual components of binary systems such as effective temperature  $T_{\text{eff}}$ , surface gravity  $\log g$ , projected rotational velocity  $v \sin i$  (where  $v$  is the equatorial rotational velocity and  $i$  is the inclination angle between the rotational axis and the line-of-sight), metallicity [Fe/H], and heliocentric radial velocity  $V_{\text{hel}}$ , as well as the colour excess  $E(B - V)$  of the system. FBS simultaneously approximates the observed spectrum by a model, which is obtained by interpolating over the grid of theoretically calculated high-resolution stellar spectra, and convolves it with a function that takes into account the broadening and wavelength shift of lines caused, respectively, by stellar rotation and motion along the line-of-sight at a given epoch. In case of a single star or a binary with a degenerate companion, the fitting routine uses one model spectrum for the single/non-degenerate star.

We separately fitted the available four wide-range spectra of 2dFS 3831 with the synthetic spectra from the TLUSTY models (Lanz & Hubeny 2003, 2007) that were convolved to the spectral resolution of each particular observation. The results of the fit of two of them are presented in Fig. 6, while mean values of the parameters determined from the fit of all four spectra are listed in Tables 3. Note that the obtained value of metallicity of 2dFS 3831 agrees fairly well with the metallicity of the SMC of  $-1.25 \pm 0.01$  dex (Cioni 2009). Note also that the rotational velocity estimate should be considered with caution because it was obtained from the low-resolution spectra and because FBS does not take into

**Table 3.** Parameters of 2dFS 3831.

Parameter	Value
$T_{\text{eff}}$ (K)	$25\,000 \pm 770$
$\log g$	$2.7 \pm 0.2$
[Fe/H]	$-1.40 \pm 0.04$
$v \sin i$ ( $\text{km s}^{-1}$ )	$580 \pm 60$
$E(B - V)$ (mag)	$0.27 \pm 0.05$

account the line broadening due to macroturbulence. On the other hand, the independent estimate of  $v \sin i$  of  $450 \text{ km s}^{-1}$  based on better spectroscopic data and the state-of-the-art stellar atmosphere models (Ramachandran et al. 2019) is not much less than our estimate. Since accounting for the effect of macroturbulence cannot significantly reduce these velocity estimates (e.g. Grassitelly et al. 2016), it is reasonable to assume that the axis of rotation of the circumstellar disk is tilted at a significant angle to our line-of-sight, which is at variance with the suggestion by González-Galán et al. (2018) that the disk is oriented face-on.

Using the last two spectra of 2dFS 3831 we measured  $\text{EW}(\text{H}\alpha)$  and found that it was equal to  $-31.8 \pm 0.5 \text{ \AA}$  and  $-34.7 \pm 0.2 \text{ \AA}$  in 2018 and 2020, respectively. A comparison of these values with the EWs measured in 1999–2016 (see Table 4) shows that the absolute value of  $\text{EW}(\text{H}\alpha)$  has reached a low in 2018 and then began to increase again. The changes in EW may reflect changes in the size/geometry of the circumstellar (excretion) disk around 2dFS 3831 caused by the feedback from the companion neutron star (e.g. Reig, Fabregat & Coe 1997) and/or by the variable mass loss from the Be star (e.g. Rajoelimanana, Charles & Udalski 2011).

To search for possible correlation between the changes in  $\text{EW}(\text{H}\alpha)$  and the binary orbital period  $P_{\text{orb}}$ , we first re-evaluated  $P_{\text{orb}}$  using the latest light curve of 2dFS 3831 from the Optical Gravitational Lensing Experiment<sup>2</sup> (OGLE; Udalski 2008). This light curve covers the time period from 2010 August 6 to 2020 January 27 (see the left-hand panel

<sup>2</sup> <http://ogle.astrouw.edu.pl/ogle4/xrom/xrom.html>

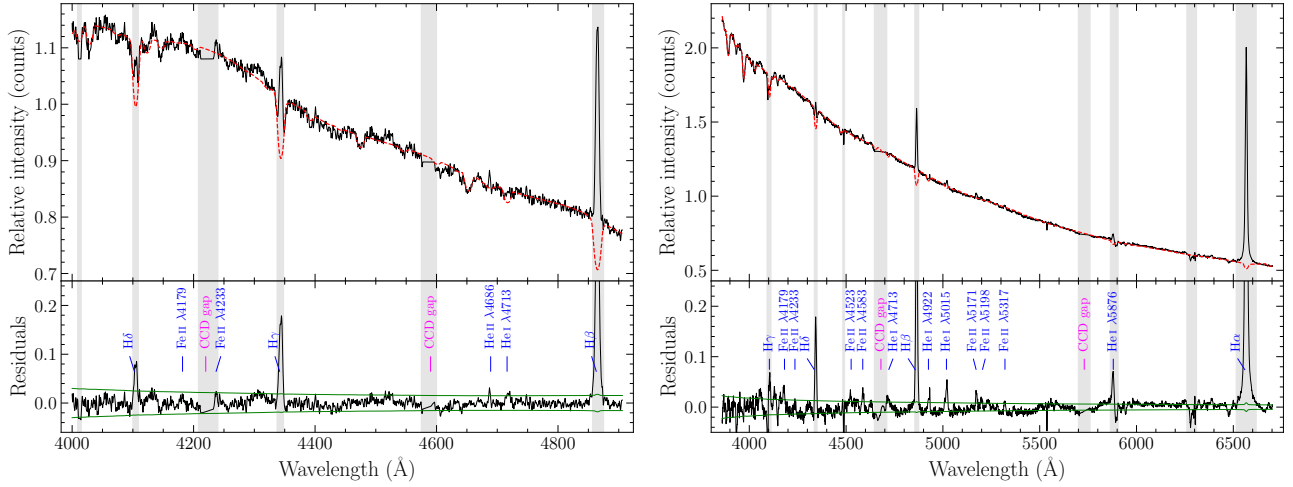


**Figure 6.** Results of modelling of two spectra of 2dFS 3831 obtained on 2014 June 17 (left-hand panel) and 2020 December 24 (right-hand panel). Upper panels: comparison of the observed spectra (solid black lines) with the best-fitting models (red dashed lines) obtained with the FBS software. The grey vertical areas show spectral regions excluded from the spectral fit because of their contamination by emission from the circumstellar disk. Bottom panels: the difference between the observed and model spectra (black noisy line). The green solid lines indicate  $1\sigma$  errors in the observed spectrum. Note that weak emission lines became more noticeable after the model subtraction. The positions of identified emission lines and CCD gaps are indicated.

**Table 4.** Changes in EW( $H\alpha$ ) with the orbital phase in the spectra of 2dFS 3831.

Date	MJD	EW( $\text{\AA}$ )	Reference	Phase
1999 September 15	51436	$-23 \pm 1$	Hénault-Brunet et al. (2012)	0.194
2012 October 13	56214	$-26.7 \pm 0.1$	Sturm et al. (2013)	0.089
2014 June 20	56829	$-36.3 \pm 0.6$	González-Galán et al. 2018	0.026
2014 June 27	56835	$-34.0 \pm 0.6$	González-Galán et al. 2018	0.036
2014 July 9	56847	$-34.1 \pm 0.6$	González-Galán et al. 2018	0.054
2016 November 2	57694	$-33 \pm 1$	González-Galán et al. 2018	0.345
2018 December 21	58474	$-31.8 \pm 0.5$	this work	0.535
2020 December 24	59207	$-34.7 \pm 0.2$	this work	0.654

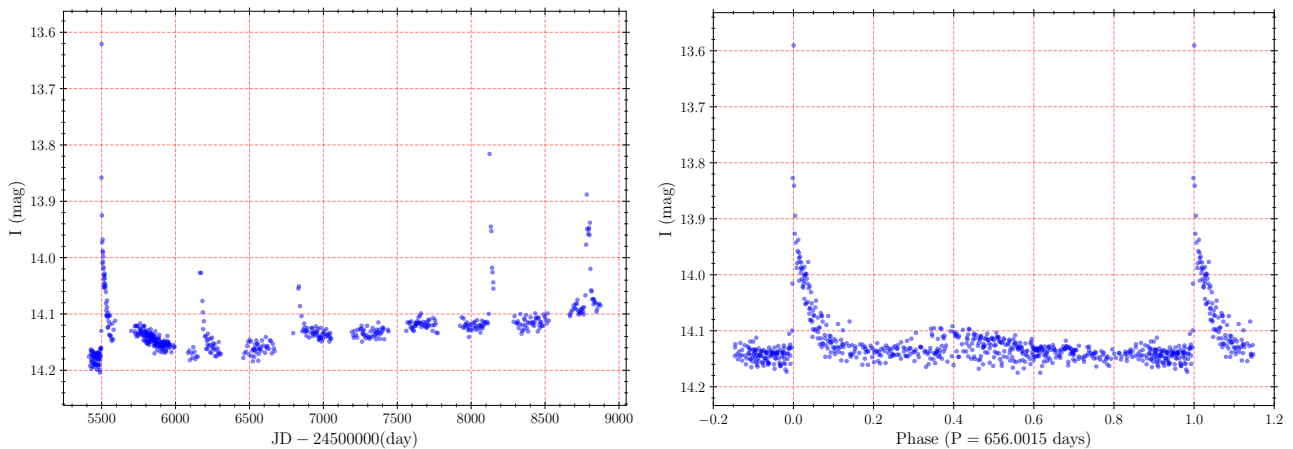


**Figure 7.** Left-hand panel: OGLE  $I$ -band light curve of 2dFS 3831 in 2010–2020. Note the gradual increase of the quiescent  $I$ -magnitude with time. Right-hand panel: The light curve folded with a period of 656.0015 d and corrected for the linear increase of the quiescent  $I$ -magnitude (see text for details).

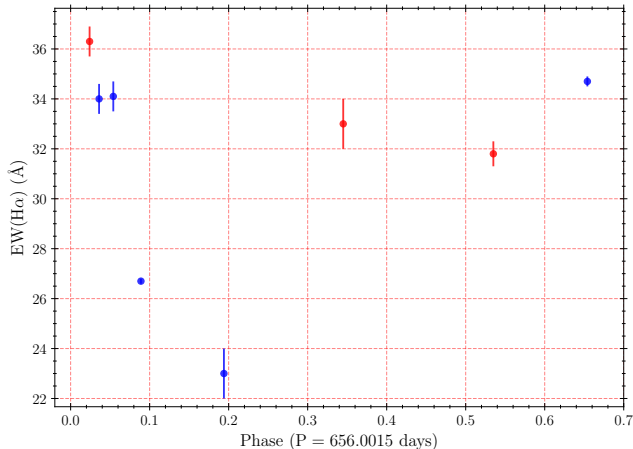


**Figure 8.** Changes in  $\text{EW}(\text{H}\alpha)$  with the orbital phase. The red data points correspond to observations where only spectral regions around the  $\text{H}\alpha$  line were obtained.

of Fig. 7), during which the system has experienced six outbursts, one of which was not covered because it fell in the gap between observations. Note that the light curve shows a clear trend of gradual increase of the quiescent  $I$ -magnitude with time (the possible existence of this trend was previously pointed out by González-Galán et al. 2018). After correction of the OGLE photometry for this trend (interpolated with a first-order polynomial function), we used the method from Lafler & Kinman (1965), that was implemented for our project of study of long-period eclipsing binaries (Knizhev et al. 2020), to derive  $P_{\text{orb}} = 656.0015 \pm 0.0015$  d with the epoch of maximum light at  $\text{JD } 2455499.5823 \pm 0.0015$ . The obtained result is in excellent agreement with the orbital ephemerides of SXP 1062 from Schmidtke et al. (2019), which are based on the OGLE light curve covering the first four observed outbursts. The light curve folded with  $P_{\text{orb}}$  is shown in the right-hand panel of Fig. 7.

Using the obtained orbital ephemerides of SXP 1062, we plot  $\text{EW}(\text{H}\alpha)$  as a function of the orbital phase (see Fig. 8). One can see that after the periastron passage of the neutron star the  $\text{EW}$  of the  $\text{H}\alpha$  line drops by about 40 per cent in  $\approx 130$  d and then almost returned to its original value in the next  $\approx 100$  d. We propose that this behaviour of  $\text{EW}(\text{H}\alpha)$  reflects the partial destruction (or changes in the geometry) of the circumstellar disk caused by the passage of the neutron star through it and its restoration in the following few months. It also turned out that the periastron passage of the neutron star led to other changes in the spectrum of 2dFS 3831. In particular, we found that in the blue spectrum obtained closest to the periastron epoch (phase 0.036), there is a noticeable emission line of  $\text{He II } \lambda 4686$  (see the left-hand panel of Fig. 6), which disappeared in the spectrum obtained about two weeks later (phase 0.054). We also found that in the spectrum obtained at the greatest distance from the periastron (phase 0.654), numerous emission lines of  $\text{Fe II}$  appeared (see the right-hand panel of Fig. 6), which were absent in other spectra. We interpret these changes in the spectrum as a consequence of the heating of the circumstellar disk due to the passage of the neutron star through it and its subsequent cooling.

**Table 5.** Changes in the heliocentric radial velocity of 2dFS 3831.

Date	$V_{\text{hel}}$ ( $\text{km s}^{-1}$ )	Phase
2012 October 13	$184 \pm 5$	0.089
2014 June 27	$206 \pm 5$	0.036
2014 July 9	$180 \pm 5$	0.054
2020 December 24	$170 \pm 20$	0.654

On a related note, using the four available wide-range spectra, we measured the heliocentric radial velocity,  $V_{\text{hel}}$ , of 2dFS 3831 (see Table 5). The mean value of these measurements of  $185 \pm 5 \text{ km s}^{-1}$  is close to the systemic velocity of the SNR shell ( $190 \pm 5 \text{ km s}^{-1}$ ) and that of the background  $\text{H}\alpha$  emission ( $188 \pm 6 \text{ km s}^{-1}$ ), which could mean that the post-SN binary obtained a low or zero kick velocity along our line-of-sight. At the same time, one can see that  $V_{\text{hel}}$  measured on 2014 June 27 (i.e. soon after the periastron passage) differs from the mean value by  $4\sigma$ . This may be due to some error in the data processing, but we consider this unlikely. Our preference is that the noticeable increase in the radial velocity near the periastron is due to the high eccentricity of the binary orbit. This can be tested by additional radial velocity measurements.

Finally, we note that the maximum value of the absolute value of  $\text{EW}(\text{H}\alpha)$  (measured for 2dFS 3831 in 2014) and the  $P_{\text{orb}} - \text{EW}(\text{H}\alpha)$  diagram by Reig et al. (1987) imply that the orbital period of SXP 1062 should be  $\approx 150$  d, which is a factor of 4 smaller than the observed value. This suggests that the radial size of the disk is not limited by the interaction with the neutron star, but by some other factor. We speculate that the equatorial spread of the excretion disk might be inhibited by the high thermal pressure in the SNR interior.

## 5 DISCUSSION

The measured expansion velocity of the optical shell of  $V_{\text{sh}} \approx 140 \text{ km s}^{-1}$  and a lace appearance of this shell are typical of SNRs in the radiative (or snow-plough) phase (e.g. Lozinskaya 1992). If MCSNR J0127–7332 is indeed in the radiative phase, then the expansion velocity of the SN blast wave  $V_{\text{SNR}}$  is equal to  $V_{\text{sh}}$ .

Let us compare the observed line ratios listed in Table 2 with the theoretical ones calculated by Allen et al. (2008) for shock models with the SMC abundances<sup>3</sup> (see their models started with the letter P). A detailed comparison showed that the observed line ratios taken together do not fit any model. Namely, while the velocity sensitive line ratios, such as  $[\text{O I}]/\text{H}\alpha$  and  $[\text{O II}]/\text{H}\beta$ , clearly indicate that the shock velocity is  $\approx 100 - 150 \text{ km s}^{-1}$ , the high value of the  $[\text{O III}]/\text{H}\beta$  ratio requires much higher shock velocities. Also, although the  $[\text{S II}]/\text{H}\alpha$  ratio in region A could be produced by fast ( $\geq 250 \text{ km s}^{-1}$ ) shocks with high values of the magnetic parameter, the much lower value of this ratio measured for region B does not fit any of the models. It should be noted, however, that the models by Allen et al. (2008)

<sup>3</sup> <http://cdsweb.u-strasbg.fr/~allen/shock.html>

consider the ionizing radiation emitted only by the shocks themselves (i.e. autoionizing shocks) and did not account for possible presence of other sources of this radiation, such as the donor stars of high-mass X-ray binaries associated with SNRs and/or OB stars in the close environments of SNRs.

The contradiction between the SNR expansion velocity estimates based on different line ratios can be avoided if some oxygen in the local ISM is doubly ionized. In this case, even a slow shock wave can produce strong [O III] lines (Raymond 1979). Similarly, the very low [S II]/H $\alpha$  ratio could be understood if a significant part of sulfur in the preshock gas is photoionized to S<sup>++</sup>. If MCSNR J0127–7332 is indeed in a radiative phase, then its slow blast wave does not produce a notable photoionized precursor (e.g. Dopita & Sutherland 1996). Thus, one needs to assume that the preshock gas is ionized by radiation from the central star of the SNR and/or OB stars in its environs (cf. Section 2). In this connection, we note that a small value of the [S II]/H $\alpha$  ratio was also found in MCSNR J0103–7201 (Gvaramadze et al. 2019), which along with MCSNR J0127–7332 are the only two known SNRs in the SMC associated with a BeXB. For MCSNR J0103–7201 we found the expansion velocity of  $\sim 100 \text{ km s}^{-1}$  (Gvaramadze et al. 2019), which is too low to explain the presence of the strong [O III]  $\lambda 5007$  emission line in the spectrum of this SNR ([O III]/H $\beta \approx 2 - 3.5$ ). We speculate that the environs of both these SNRs are ionized by their central stars. This possibility, however, has to be proved by further research.

Our estimate of the SNR expansion velocity is a factor of three lower than the expansion velocity derived by Hénault-Brunet et al. (2012) and the one following from the X-ray spectral modelling by Haberl et al. (2012). Let us discuss this discrepancy.

Both Hénault-Brunet et al. (2012) and Haberl et al. (2012) assumed that MCSNR J0127–7332 is in the Sedov (adiabatic) phase. Apparently, their assumption is based on the widely accepted hypothesis by McKee & Cowie (1975) “that all the optically observed SNRs are still in the adiabatic phase of their expansion”, which was put forward to explain correlation between optical and X-ray emission in the SNR Cygnus Loop. This hypothesis suggests that the SN blast wave in Cygnus Loop propagates in a cloudy medium, and that the optical emission in this SNR is produced by radiative shocks in dense cloudlets, while the X-ray emission originates in the lower-density intercloud medium shocked by the adiabatic blast wave (McKee & Cowie 1975; Bychkov & Pikelner 1975). Correspondingly, it is assumed that the expansion velocity of the SN blast wave,  $V_{\text{SNR}}$ , is related to the temperature of the X-ray emitting plasma,  $T_X$ , through the following equation:  $V_{\text{SNR}} = 920 \text{ km s}^{-1} (T_X/1 \text{ keV})^{1/2}$ . [Note that application of this equation to MCSNR J0127–7332 with its  $T_X = 0.23 \text{ keV}$  (Haberl et al. 2012) yields  $V_{\text{SNR}} = 440 \text{ km s}^{-1}$ .] Also, since radial velocity measurements indicate (e.g. Minkowski 1958) that the optically-emitting shell in Cygnus Loop is expanding at a lower velocity than that inferred from X-ray observations (Tucker 1971), it was suggested (McKee & Cowie 1975) that the shocked cloudlets are accelerated by the SN blast wave to a fraction of its velocity.

Although the above consideration allows to explain the discrepancy between estimates of the SNR expansion velocity based on X-ray and optical observations, it faces a problem in explaining the shape of the optical filaments,

which are actually bumpy thin sheets viewed at different angles (Hester 1987). To avoid this problem, McKee & Cowie (1975) suggested that the cloudlets must have at least one small dimension, i.e. they should be in the form of sheets. It remains unclear, however, what the origin of these sheet-like cloudlets and why they “have arranged themselves in such a nicely spherical shell” (McCray & Snow 1979) such as observed in Cygnus Loop (and some other SNRs, like Vela, S147, etc.). The answer suggested by McCray & Snow (1979; cf. Charles, Kahn & McKee 1985) is that Cygnus Loop was produced by the SN progenitor star and not by the SN itself, meaning that the SN exploded in a cavity, evacuated by the stellar wind of the SN progenitor (cf. Gvaramadze et al. 2017).

This idea was explored in detail by a number of workers (e.g. Ciotti & D’Ercole 1988; Tenorio-Tagle et al. 1991; Franco et al. 1991), who modelled a SN explosion in a wind-driven bubble created by the SN progenitor star. Particularly, it was shown that the evolution of the SN blast wave depends on the mass of the shell surrounding the bubble. In the case when the mass of this wind-driven shell (WDS) is more than 50 times greater than the mass of the SN ejecta,  $M_{\text{ej}}$ , the SN blast wave merges with the WDS and the resulting SNR skips the Sedov phase and enters directly in the radiative phase (e.g. Franco et al. 1991), meaning that  $V_{\text{SNR}}$  is equal to the expansion velocity of the optically-emitting shell  $V_{\text{sh}}$ . In this process, the former WDS (now the SNR shell) acquires a kinetic energy of  $E_{\text{kin}} = M_{\text{sh}} V_{\text{sh}}^2 / 2 \approx (0.1 - 0.3) E_{\text{SN}}$ , where  $M_{\text{sh}} \approx (4\pi/3) R_{\text{sh}}^3 m_{\text{H}} n_{\text{ISM}}$  is the mass of the WDS (i.e. the mass of the ISM gas originally contained within a sphere of radius  $R_{\text{sh}}$ ),  $R_{\text{sh}}$  is the radius of the WDS,  $m_{\text{H}}$  is the mass of the hydrogen atom,  $n_{\text{ISM}}$  is the number density of the local ISM, and  $E_{\text{SN}}$  is the energy of the SN blast wave (Franco et al. 1991). Moreover, the collision of the SN blast wave with the WDS leads to the development of the Rayleigh-Taylor instability, resulting in dome-like deformations of the shell which, when viewed from different angles, determine the lace appearance of some SNRs, such as Vela and S147 (Gvaramadze 1999, 2006). On the other hand, the inner layers of the shocked WDSs could be hot enough to produce soft X-ray emission (e.g. Tenorio-Tagle et al. 1991).

Based on the above, we propose that MCSNR J0127–7332 is the result of SN explosion in a cavity surrounded by a massive WDS. This proposal provides a natural explanation of the coexistence of the slowly expanding optical shell and the soft X-ray emission within it. Assuming that the size of the SNR is equal to the size of the WDS, i.e.  $R_{\text{SNR}} \approx R_{\text{sh}}$  (so that the mass of the SNR shell is equal to the mass of the pre-existing WDS), and adopting  $E_{\text{SN}} = 10^{51} \text{ erg}$  and  $E_{\text{kin}} = (0.1 - 0.3) E_{\text{SN}}$ , one finds that  $M_{\text{sh}} \approx 500 - 1500 M_{\odot}$  and  $n_{\text{ISM}} \approx 0.4 - 1.2 \text{ cm}^{-3}$ . Correspondingly, the age of MCSNR J0127–7332 is approximately equal to the crossing time of the wind bubble, i.e.  $t_{\text{SNR}} \sim R_{\text{SNR}} / V_{\text{ej}}$ , where  $V_{\text{ej}} = (2E_{\text{SN}} / M_{\text{ej}})^{1/2}$  is the velocity of the SN ejecta of mass  $M_{\text{ej}}$ . To estimate  $M_{\text{ej}}$ , we assume that the SN explosion was symmetric (i.e. no natal kick was imparted to the new-born neutron star) and that the current orbital eccentricity,  $e$ , of SXP 1062 did not change much since the SN explosion. In this case, one finds (e.g. Iben & Tutukov 1997) that  $M_{\text{ej}} = e(M_* + M_{\text{NS}})$ , where  $M_*$  and  $M_{\text{NS}}$  are the masses of 2dFS 3831 and its companion neutron star, respectively. Adopting  $M_* = 15 M_{\odot}$

(Hénault-Brunet et al., 2012) and  $M_{\text{NS}} = 1.4 M_{\odot}$ , one finds that  $V_{\text{ej}} \gtrsim 2700 e^{-1/2} \text{ km s}^{-1}$  and  $t_{\text{SNR}} \lesssim 8000 e^{1/2} \text{ yr}$ . We caution, however, that these estimates should be regarded only as rough order-of-magnitude values.

## 6 SUMMARY

We have presented the results of optical spectroscopic observations of the SNR MCSNR J0127–7332 in the SMC and the mass donor star, 2dFS 3831, of its associated BeXB SXP 1062 carried out with the Southern African Large Telescope (SALT). The long-slit SALT spectroscopy of the SNR shell allowed us to measure its expansion velocity of  $\approx 140 \text{ km s}^{-1}$ , which is typical of SNRs in the radiative (snow-plough) phase. A comparison of the line ratios in the spectrum of the SNR shell with the library of line intensities for shock models (MAPPINGS III) showed that the observed line ratios taken together did not fit any model. It was suggested that these ratios can be explained if the local ISM is ionized by 2dFS 3831 and/or by OB stars in the vicinity of the SNR. To reconcile the coexistence of the slowly expanding optical shell of the SNR and the soft X-ray emission within it, it was proposed that the SN explosion occurred within a cavity evacuated by the wind of the SN progenitor star and that the cavity at the moment of SN explosion was surrounded by a massive shell (more than 50 times more massive than the SN ejecta). This proposal implies the age of the SNR of  $\lesssim 10,000 \text{ yr}$ .

Spectroscopic observations of 2dFS 3831 has revealed that EW of the  $\text{H}\alpha$  emission line decreased by about 40 per cent in  $\approx 130 \text{ d}$  after the periastron passage of the neutron star and then almost returned to its original value in the next  $\approx 100 \text{ d}$ . These changes in EW are accompanied by other changes in the spectral appearance of the Be star: in the spectrum obtained shortly after the periastron, there was a noticeable emission line of  $\text{He II } \lambda 4686$ , which disappeared in the next two weeks or so. We interpreted these changes as the result of the interaction of the neutron star with the circumstellar disk which led to a temporary disturbance and heating of the disk. We also found an indication that the neutron star orbits 2dFS 3831 in a highly eccentric orbit, but additional high-resolution spectra covering all orbital phases of the binary system are needed to confirm this.

## 7 ACKNOWLEDGEMENTS

This work is based on observations obtained with the Southern African Large Telescope (SALT), under programs 2012-1-RSA-UKSC-003, 2014-1-RSA.OTH-022, 2016-2-SCI-044, 2018-1-MLT-008 and 2020-1-MLT-003. VVG acknowledges support from the Russian Science Foundation under grant 19-12-00383. A.Y.K. acknowledges support from the National Research Foundation (NRF) of South Africa. LMO acknowledges partial support by the Russian Government Program of Competitive Growth of Kazan Federal University. This research has made use of the SIMBAD data base, operated at CDS, Strasbourg, France.

## 8 DATA AVAILABILITY

The data underlying this article will be shared on reasonable request to the corresponding author.

## REFERENCES

- Allen M. G., Groves B. A., Dopita M. A., Sutherland R. S., Kewley L. J., 2008, *ApJS*, 178, 20
- Buckley D. A. H., Swart G. P., Meiring J. G., 2006, in Stepp L. M., ed., *Proc. SPIE Conf. Ser. Vol. 6267, Ground-based and Airborne Telescopes*. SPIE, Bellingham, p. 62670Z
- Burgh E. B., Nordsieck K. H., Kobulnicky H. A., Williams T. B., O’Donoghue D., Smith M. P., Percival J. W., 2003, in Iye M., Moorwood A. F. M., eds, *Proc. SPIE Conf. Ser. Vol. 4841, Instrument Design and Performance for Optical/Infrared Ground-based Telescopes*. SPIE, Bellingham, p. 1463
- Bychkov K. V., Pikelner S. B., 1975, *Soviet Astron. Lett.*, 1, 14
- Charles P. A., Kahn S. M., McKee C. F., 1985, *ApJ*, 295, 456
- Cioni M.-R. L., 2009, *A&A*, 506, 1137
- Ciotti L., D’Ercole A., 1989, *A&A*, 215, 347
- Corbet R. H. D. et al., 2016, *ApJ*, 829, 105
- Crawford S. M. et al., 2010, in Silva D. R., Peck A. B., Soifer B. T., *Proc. SPIE Conf. Ser. Vol. 7737, Observatory Operations: Strategies, Processes, and Systems III*. SPIE, Bellingham, p. 773725
- Dopita M. A., Sutherland R. S., 1996, *ApJSS*, 102, 161
- Fesen R. A., Blair W. P., Kirshner R. P., 1985, *ApJ*, 292, 29
- Franco J., Tenorio-Tagle G., Bodenheimer P., Różyczka M., 1991, *PASP*, 103, 803
- Frew D. J., Parker Q. A., 2010, *PASA*, 27, 129
- Fulmer L. M., Gallagher J. S., Hamann W.-R., Oskinova L. M., Ramachandran V., 2020, *A&A*, 633, A164
- Georgelin Y. M., Georgelin Y. P., Laval A., Monnet G., Rosado M., 1983, *A&AS*, 54, 459
- González-Galán A., Oskinova L. M., Popov S. B., Haberl F., Kühnel M., Gallagher J., Schurch M. P. E., Guerrero M. A., 2018, *MNRAS*, 475, 2809
- Grassitelli L., Fossati L., Langer N., Simón-Díaz S., Castro N., Sanyal D., 2016, *A&A*, 593, A14
- Gvaramadze V. V., 1999, *A&A*, 352, 712
- Gvaramadze V. V., 2006, *A&A*, 454, 239
- Gvaramadze V. V. et al., 2017, *Nat. Astron.*, 1, 0116
- Gvaramadze V. V., Kniazev A. Y., Oskinova L. M., 2019, *MNRAS*, 485, L6
- Haberl F., Sturm R., 2016, *A&A* 586, A81
- Haberl F., Sturm R., Filipović M. D., Pietsch W., Crawford E. J., 2012, *A&A*, 537, L1
- Heinz S. et al., 2013, *ApJ*, 779, 171
- Hénault-Brunet V. et al., 2012, *MNRAS*, 420, L13
- Hester, J. J., 1987, *ApJ*, 314, 187
- Hilditch R. W., Howarth I. D., Harries T. J., 2005, *MNRAS*, 357, 304
- Ho W. C. G., Wijngaarden M. J. P., Andersson N., Tauris T. M., Haberl F., 2020, *MNRAS*, 494, 44
- Iben I., Tutukov A. V., 1997, *ApJ*, 491, 303
- Kniazev A. Y., Pustilnik S. A., Grebel E. K., Lee H., Pramskij A. G., 2004, *ApJS*, 153, 429
- Kniazev A. Y. et al., 2008, *MNRAS*, 388, 1667
- Kniazev A. Y., Malkov O. Y., Katkov I. Y., Berdnikov L. N., 2020, *RAA*, 20, 119
- Kobulnicky H. A., Nordsieck K. H., Burgh E. B., Smith M. P., Percival J. W., Williams T. B., O’Donoghue D., 2003, in Iye M., Moorwood A. F. M., eds, *Proc. SPIE Conf. Ser. Vol. 4841, Instrument Design and Performance for Opti-*

- cal/Infrared Ground-based Telescopes. SPIE, Bellingham, p. 1634
- Kopsacheili M., Zezas A., Leonidaki I., 2020, MNRAS, 491, 889
- Lafier J., Kinman T. D., 1965, ApJS, 11, 216
- Lanz T., Hubeny I., 2003, ApJS, 146, 417
- Lanz T., Hubeny I., 2007, ApJS, 169, 83
- Leonidaki I., Boumis P., Zezas A., 2013, MNRAS, 429, 189
- Linares M. et al., 2010, ApJ, 719, L84
- Lozinskaya T. A., 1992, *Supernovae and Stellar Wind in the Interstellar Medium*. Am. Inst. Phys., New York
- Maitra C. et al., 2019, MNRAS, 490, 5494
- Mathewson D. S., Clarke J. N., 1973, ApJ, 180, 725
- McCray R., Snow T. P., Jr, 1979, ARA&A, 17, 213
- McKee C. F., Cowie L. L., 1975, ApJ, 195, 715
- Minkowski R., 1958, Rev. Mod. Phys., 30, 1048
- Nigra L., Gallagher J. S., Smith L. J., Stanimirović S., Nota A., Sabbi E., 2008, PASP, 120, 972
- O'Donoghue D. et al., 2006, MNRAS, 372, 151
- Rajoelimanana A. F., Charles P. A., Udalski A., 2011, MNRAS, 413, 1600
- Ramachandran V., et al., 2019, A&A, 625, A104
- Raymond J. C., 1979, ApJS, 39, 1
- Reig P., Fabregat J., Coe M. J., 1997, A&A, 322, 193
- Rosado M., Georgelin Y. M., Laval A., Monnet G., 1983, in Gorenstein P., Danziger I. J., eds, Proc. IAU Symp. 101, *Supernova Remnants and Their X-ray Emission*. Reidel, Dordrecht, p. 567
- Schmidtke P. C., Cowley A. P., Udalski A., 2012, Astron. Telegram, 4596, 1
- Schmidtke P. C., Cowley A. P., Udalski A., 2019, The Astronomer's Telegram, 13426, 1
- Seward F. D., Charles P. A., Foster D. L., Dickel J. R., Romero P. S., Edwards Z. I., Perry M., Williams R. M., 2012, ApJ, 759, 123
- Sturm R., Haberl F., Oskinova L. M., Schurch M. P. E., Hénault-Brunet V., Gallagher J. S., Udalski A., 2013, A&A, 556, A139
- Tauris T. M., van den Heuvel E. P. J., 2006, in Lewin W. H. G., van der Klis M., eds, *Formation and Evolution of Compact Stellar X-ray Sources*, Compact stellar X-ray sources. Cambridge Univ. Press, Cambridge, p. 623
- Tenorio-Tagle G., Różyczka M., Franco J., Bodenheimer P., 1991, MNRAS, 251, 318
- Tucker W. H., 1971, Science, 172, 372
- Udalski A., 2008, Acta Astron., 58, 187
- van Soelen B., Komin N., Kniazev A., Väisänen P., 2019, MNRAS, 484, 4347
- Wang W., Tong H., 2020, MNRAS, 492, 762